

MTVNet: Mapping using Transformers for Volumes – Network for Super-Resolution with Long-Range Interactions

August Leander Høeg, Sophia W. Bardenfleth, Hans Martin Kjer, Tim B. Dyrby,
 Vedrana Andersen Dahl, Anders Dahl
 Visual Computing, Technical University of Denmark
 {aulho, soeba, hmkj, tbdy, vand, abda}@dtu.dk

Abstract

Until now, it has been difficult for volumetric super-resolution to utilize the recent advances in transformer-based models seen in 2D super-resolution. The memory required for self-attention in 3D volumes limits the receptive field. Therefore, long-range interactions are not used in 3D to the extent done in 2D and the strength of transformers is not realized. We propose a multi-scale transformer-based model based on hierarchical attention blocks combined with carrier tokens at multiple scales to overcome this. Here information from larger regions at coarse resolution is sequentially carried on to finer-resolution regions to predict the super-resolved image. Using transformer layers at each resolution, our coarse-to-fine modeling limits the number of tokens at each scale and enables attention over larger regions than what has previously been possible. We experimentally compare our method, MTVNet, against state-of-the-art volumetric super-resolution models on five 3D datasets demonstrating the advantage of an increased receptive field. This advantage is especially pronounced for images that are larger than what is seen in popularly used 3D datasets. Our code is available at <https://github.com/AugustHoeg/MTVNet>.

1. Introduction

In recent years, super-resolution (SR) and other vision tasks have seen significant improvements via usage of vision transformers (ViTs). Although ViTs achieve state-of-the-art (SOTA) performance in 2D SR [12, 16, 29, 39], few studies have attempted applying ViTs for volumetric SR. Part of the success of ViTs is their increased receptive field compared to Convolutional Neural Networks (CNNs), enabling inferences based on broader image context [20]. In volumetric SR, ViTs are challenged by the cubic growth in tokens required to process larger 3D image contexts. Although window-based attention improves the quadratic complexity

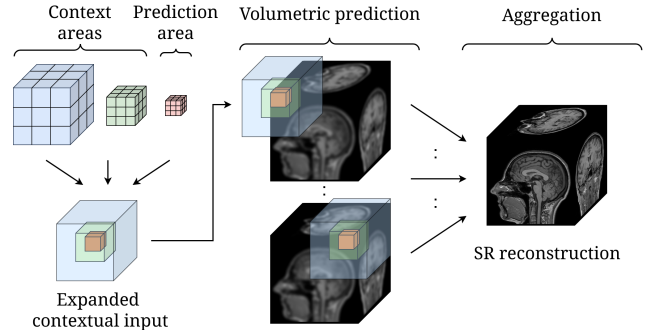


Figure 1. Overview of MTVNet that is informed by a large contextual volume processed at multiple resolution scales for predicting SR in the center volume.

of attention mechanisms [41], the complexity of 3D data still limits the receptive field of volumetric ViT-based models. Because of this disadvantage, the performance gap of CNNs vs. transformer-based architectures for volumetric SR has yet to be fully understood.

Several works have studied visual enhancement of 3D medical data such as MRI (magnetic resonance imaging) and CT (computed tomography) by upscaling each slice independently [33, 45, 52, 60, 65]. While such approaches circumvent the complexity issues of volumetric SR, not fully considering the 3D context sacrifices performance and risks inter-slice discontinuities [13–15, 22, 47].

Current brain MRI benchmark datasets for evaluating volumetric SR are relatively low-resolution [32], limiting the benefits of a larger receptive field. Advancements in medical imaging technology enable higher spatial resolution [63], resulting in larger volumes where volumetric SR can benefit from long-range contextual information. Given the potential of SR in clinical settings and the increasing interest in applications like multi-resolution synchrotron imaging [57], there is a need for volumetric SR methods designed specifically for high-resolution (HR) 3D data.

Aside increasing contextual information in volumetric

SR, recent studies in 2D SR have shown that the window-based attention mechanism of the Swin-Transformer [41] is not ideal for capturing relationships across distant image regions. Using Local Attribution Mapping (LAM), Chen et al. [12] showed that strengthening long-range information exchange can lead to significant performance gains. Similarly, recent studies in ViT architectures have focused on modeling long-range interactions to increase performance [9, 28].

To address these limitations, we present MTVNet, a volumetric SR approach based on multi-scale image representation and hierarchical attention to enhance long-range information propagation. Our MTVNet broadens the receptive field by expanding the contextual input beyond the prediction area, see Fig. 1. We hypothesize that for the SR task, image regions near the prediction region provide the most important contextual information while more distant regions still provide relevant information, but contribute less. Consequently, we design a coarse-to-fine feature extraction and tokenization scheme with progressively less computational resources allocated towards regions further from the prediction area, enabling us to increase the volumetric input size without exceeding GPU memory. Furthermore, inspired by FasterViT [28] and SwinV2 [42], we propose an efficient shifting hierarchical attention mechanism suitable for volumetric image processing. This approach leverages specialized carrier tokens (CATs) that contain compact feature summaries of larger attention windows. Using full attention in the highly compressed CAT domain, our model improves modeling of long-range spatial information, further improving SR performance in volumetric data.

We compare our proposed MTVNet against several volumetric SR approaches on four brain MRI benchmark datasets and one high-resolution CT based dataset. Extensive experiments show that convolutional models still outperform ViT-based architectures in lower resolution datasets. Although on high-resolution 3D data with meaningful long-range image dependencies, our proposed MTVNet outperforms all other volumetric SR approaches. We anticipate that our proposed multi-contextual approach could greatly benefit other volumetric image tasks.

2. Related Work

2.1. Learning-based super-resolution

The advantages of learning-based SR over classical interpolation methods were first demonstrated by SRCNN proposed by Dong et al. [18]. Since then, several CNN-based SR models have been proposed to improve performance and computational efficiency [19, 36, 40, 62, 67]. Despite the success of CNNs, many vision tasks such as image classification [9, 20, 28, 41], object detection [8, 24, 48, 50], segmentation [7, 10, 23, 27, 61], and SR have seen improvements using vision transformers (ViTs). SwinIR by

Liang et al. [39] were among the first to demonstrate the superiority of transformers over convolution-based models for SR by incorporating the Swin Transformer [41] in a residual network scheme. Chen et al. [11, 12] proposed cross attention of overlapping window partitions and channel attention mechanisms to enable activation of more input pixels. Chu et al. [16] suggested HMANet, which integrates a grid-shuffling scheme with window-based attention to model cross-area similarity for enhanced image reconstruction. Very recently, Hsu et al. [29] have suggested combining Swin-transformer layers and gating mechanisms in a densely-connected structure [30, 54] to alleviate information bottlenecks.

Concurrently, improvements to the vision transformer backbone have been proposed to enable efficient processing of HR image data. Liu et al. [42] proposed SwinV2, featuring improved normalization and a more efficient attention mechanism using cosine similarity. This work was later applied to SR by Conde et al. [17] in Swin2SR. In CrossViT [9], multi-scale tokenization and efficient cross-attention mechanisms were used to extract and fuse feature representations at different image scales. Recently, Hatamizadeh et al. [28] proposed FasterViT, an efficient vision transformer including local window attention and global attention. Since these models focus on 2D images, most do not scale well in 3D, requiring substantial modifications to be applied for volumetric data.

2.2. Super-resolution for 3D volumes

3D SR methods operate slice-wise or volumetric. Slice-wise methods predict each slice independently and typically leverage model architectures from 2D SR. While these models can handle entire slices simultaneously and often support deeper network architectures, they lack cross-slice information, which can lead to discontinuities between slice predictions.

Volumetric SR methods fully utilize the context in 3D, achieving better overall performance than slice-wise methods because of improved inter-plane predictions, but with much higher computational costs [13–15, 22, 47]. Inspired by SRCNN [18] and SRGAN [14], Pham et al. [46] and Chen et al. [14] proposed three-dimensional adaptations of convolutional SR models and demonstrated the potential of volumetric SR over slice-wise approaches. Research in volumetric SR has since grown rapidly and several methods have been proposed to improve efficiency and performance [13, 15, 21, 38, 43, 47, 49, 58, 64]. These approaches are very similar to classical SR in that they aim to predict HR reconstructions from isotropically degraded images, only on volumetric instead of 2D images. However, several other approaches for volumetric SR also exist. For instance, to account for the fact that clinical MR images often feature high in-plane and low through-plane resolution, axial SR mod-

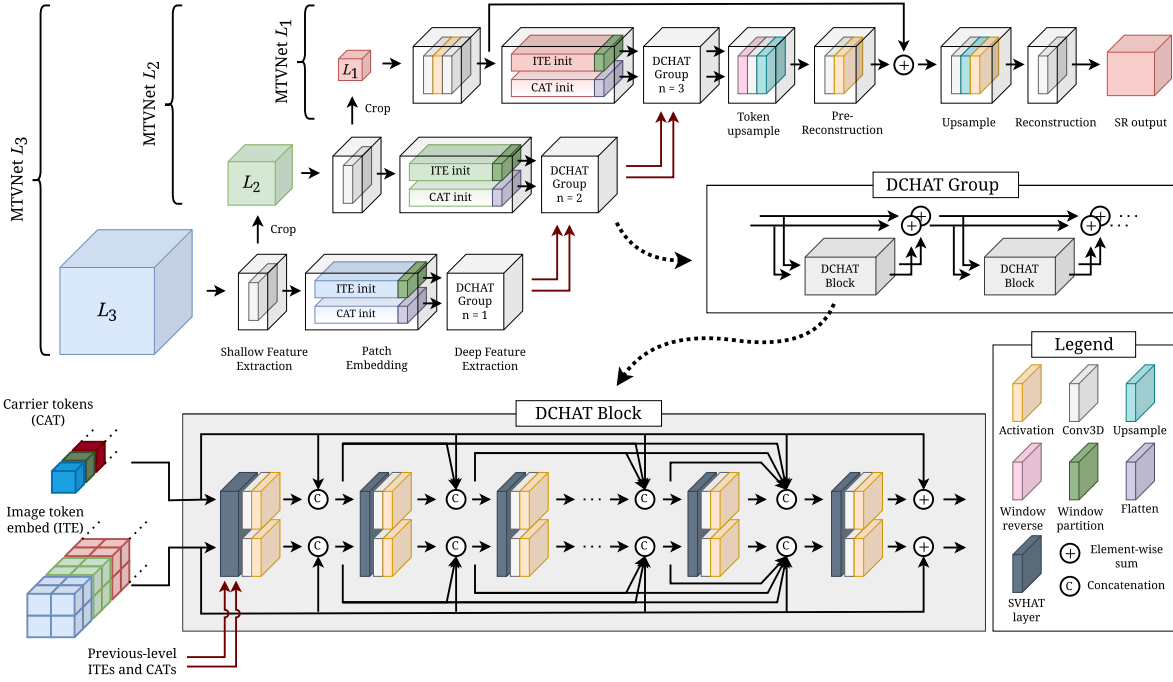


Figure 2. Illustration of MTVNet and the structure of DCHAT Block and DCHAT Group. Our proposed architecture consists of up to three levels of multi-contextual volumetric image processing. The first two levels perform tokenization using larger 3D patch sizes to cover broader contextual regions, while succeeding levels process subsets of the input volume using smaller patch sizes, resulting in both coarse- and fine-grained feature extraction. The depth of subsequent DCHAT Groups increases from $n = 1$ to 3 DCHAT Blocks towards the last stage. The token embeddings from preceding network levels are fused into later levels using cross attention.

els [25, 31, 59] have been proposed to increase slice count while preserving in-plane resolution.

To alleviate the limitation of fixed upscaling factors, arbitrary scale SR based on Implicit Neural Representation [64] [68] [37] have been proposed. Another branch of volumetric SR is multi-contrast models [31, 37] that leverage information from multiple MRI modalities (T1- and T2-weighted images).

Transformer-based architectures have also been proposed for volumes. SuperFormer [22] merged feature embeddings and volume embeddings using a volumetric transformer-based network structure similar to SwinIR [39]. Also inspired by SwinIR, Ji et al. [31] implemented a transformer-based GAN (generative adversarial network) model for axial super-resolution using residual swin transformer blocks [39, 41]. The CFTN model [66] employed 3D residual channel attention blocks [67] and transformers to capture global cross-scale dependencies between multi-scale feature embeddings. Li et al. [37] proposed a 2D slice-wise multi-modal arbitrary scale SR model featuring a rectangle-window cross-attention transformer to model longer-range image dependencies. Despite the growing interest in volumetric transformer-based SR models, several of the improvements seen in 2D SR cannot be effectively applied in 3D due to memory limitations. Our work seeks

to leverage these developments to enhance volumetric SR while simultaneously addressing the challenge of limited contextual information, a critical bottleneck in volumetric SR.

3. Methods

3.1. Network architecture

The architecture of MTVNet consists of three levels of volumetric image processing: L_3 , L_2 , and L_1 , see Fig. 2. The network levels L_3 and L_2 extract features from image regions surrounding the SR prediction area and merges these features into L_1 . These features serve as a prior for the network level L_1 , enabling conditioning of the SR output based on the surrounding image context.

Shallow Feature Extraction. Our MTVNet uses shallow feature extraction (SFE) modules for initial processing at each level. Given an input volume $I_{LR} \in \mathbb{R}^{C_{in} \times H \times W \times D}$, each SFE module expands the channel dimension using $3 \times 3 \times 3$ convolutional layers, producing shallow features $\mathcal{F}_{SFE} \in \mathbb{R}^{C_{emb} \times H \times W \times D}$. The output from each stage's SFE is cropped and passed to the next level, allowing the model to leverage the features of previous SFE modules.

Patch embedding. During patch embedding, shallow features are projected and tokenized into differently-sized

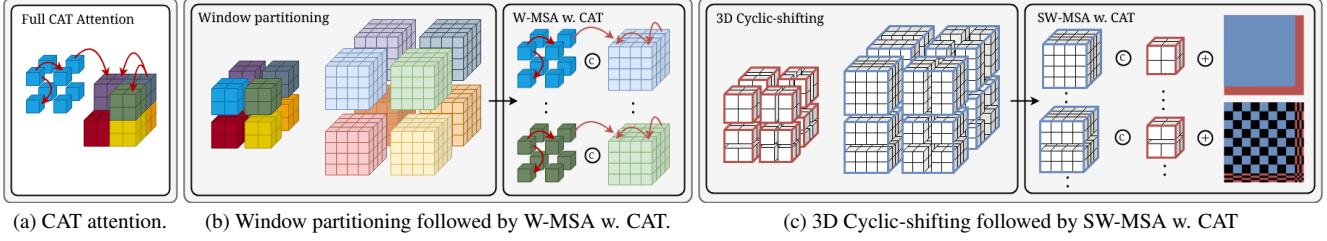


Figure 3. Illustration of volumetric attention mechanisms used in SVHAT: 3a) Full CAT attention, 3b) W-MSA with CAT and 3c) SW-MSA with CAT. Our proposed SVHAT uses alternating shifted and non-shifted windowed attention. Masking is used to limit information exchange between non-adjacent ITEs and CATs. In these examples, the window size is $M = 4$ and the CAT space size is $c = 2$.

volumetric image patches. The levels L_3 and L_2 use larger patch sizes to cover wider image regions, reducing the number of tokens required for processing these volumes. Image token embeddings (ITEs) \mathbf{x}^L are obtained via a $p_L \times p_L \times p_L$ strided convolution, where L corresponds to the network level. For subsequent processing, we partition the ITEs into attention windows of $M \times M \times M$ tokens. The corresponding carrier token embeddings (CATs) $\mathbf{x}_{\text{cat}}^L$ are initialized from the ITEs using convolution with stride and kernel size $\lfloor \frac{M}{c} \rfloor \times \lfloor \frac{M}{c} \rfloor \times \lfloor \frac{M}{c} \rfloor$, where c is a factor determining the number of CATs for each attention window.

Deep Feature Extraction. Deep feature extraction is performed within each level using DCHAT (densely connected hierarchical attention) blocks to extract high-frequency spatial information. The DCHAT blocks for each level are connected in a residual scheme to produce DCHAT groups consisting of up to three DCHAT blocks. In the case of multiple levels, cross-attention mechanisms [56] are used to merge token embeddings into subsequent network levels, facilitating the propagation of multi-scale information.

Reconstruction. In the final stage, token upsampling is performed via a deconvolution layer, transforming the patch embeddings back into the image space. These features are further refined in a pre-reconstruction stage before being fused with the shallow features through a long skip-connection. The fused features are then upsampled using a 3D pixel-shuffle layer [51]. We employ a 3D pre-convolution layer initialized according to the ICNR method described in [1] to prevent checkerboard artifacts during pixel-shuffling.

3.2. Dense-Connected Hierarchical Attention block

For efficient extraction of volumetric image features, we propose a DCHAT block, see Fig. 2. Inspired by Hsu et al. [29], our DCHAT block employs a densely connected structure of volumetric transformer layers, LeakyReLU activations, and convolutions. To preserve the feature space of ITEs and CATs, we process each set of tokens using separate sets of skip connections and convolutions. Additionally, we match the embedding dimension of ITEs and

CATs throughout each block to equally promote learning of progressively complex features. As in DRCT [29] we utilize $1 \times 1 \times 1$ convolutions as gating mechanisms between transformer layers to filter redundant features, improving efficiency and enabling feature transition between DCHAT blocks.

3.3. Shifting Hierarchical Attention Transformer

Inspired by FasterViT [28] and SwinV2 [42], we design an SVHAT (shifting volumetric hierarchical attention transformer) layer for concurrent processing of ITEs and CATs. Similar to FasterViT, SVHAT uses a combination of full attention and windowed attention to extract hierarchical image features. The attention mechanisms used in SVHAT are illustrated in Fig. 3. First, full attention in the CAT space allows global information flow across attention windows, see Fig. 3a. Next, we concatenate each attention window’s corresponding CATs and ITEs, providing each attention window access to its set of CATs. Windowed attention is then applied jointly to the ITEs and CATs to capture token dependencies, with the CATs conveying global information from other attention windows, see Fig. 3b. This alternating attention procedure allows global feature exchange between local attention windows, improving long-range information flow. To further enhance information exchange, we reintroduce shifted window-based attention into the attention framework proposed in FasterViT [28], see Fig. 3c. Before window partitioning of ITEs and CATs, we perform 3D cyclic-shifting to allow attention of tokens in neighboring windows. To account for the presence of CATs, we shift both the image space and CAT space by $\lfloor \frac{M}{2} \rfloor$ and $\lfloor \frac{c}{2} \rfloor$ voxels, respectively. This shifting conserves the alignment of the two feature spaces. Attention masking is applied to drop interactions between non-adjacent tokens in the ITE/CAT space.

We compute attended carrier token embeddings $\hat{\mathbf{x}}_{\text{cat}}^{L,t}$ at network level L and transformer layer t as follows:

$$\begin{aligned} \hat{\mathbf{x}}_{\text{cat}}^{L,t} &= \mathbf{x}_{\text{cat}}^{L,t-1} + \gamma_1 \text{MSA} \left(\text{LN} \left(\mathbf{x}_{\text{cat}}^{L,t-1} \right) \right), \\ \mathbf{x}_{\text{cat}}^{L,t} &= \hat{\mathbf{x}}_{\text{cat}}^{L,t} + \gamma_2 \text{MLP} \left(\text{LN} \left(\hat{\mathbf{x}}_{\text{cat}}^{L,t} \right) \right), \end{aligned} \quad (1)$$

where γ_1 , γ_2 are learnable channel-wise scaling factors, MSA is the multi-headed self-attention mechanism [56], LN denotes Layer Normalization [2], and MLP is the multi-layer perception.

After CAT attention, we compute attention of ITEs and CATs using windowed self-attention, see Eq. (2). The CATs are window partitioned and concatenated with their corresponding set of ITEs to produce sequences of $M^3 + c^3$ tokens for each attention window. Inspired by SwinV2 [42], SVHAT employs a post-normalized Shifted Window based Self-Attention (SW-MSA) procedure. Window-attended CATs and ITEs $\mathbf{x}_w^{L,t+1}$ are computed as:

$$\begin{aligned}\mathbf{x}_w^{L,t} &= [\mathbf{x}^{L,t-1}, \mathbf{x}_{\text{cat}}^{L,t}] \\ \hat{\mathbf{x}}_w^{L,t+1} &= \mathbf{x}_w^{L,t} + \text{LN}(\text{SW-MSA}(\mathbf{x}_w^{L,t})) \\ \mathbf{x}_w^{L,t+1} &= \hat{\mathbf{x}}_w^{L,t+1} + \text{LN}(\text{MLP}(\hat{\mathbf{x}}_w^{L,t+1}))\end{aligned}\quad (2)$$

The ITEs and CATs are then separated again to ensure compatibility with subsequent SVHAT layers.

Prior to the attention mechanisms for ITEs and CATs (described in Eq. (1) and Eq. (2)), SVHAT uses multi-head cross-attention (MCA) layers to facilitate information exchange across network levels. Each cross-attention layer implements a two-layer MLP to ensure dimension compatibility between cross-scale token sequences. Then, MCA is applied to capture relationships between current- and previous-level token embeddings. Exploiting the small size of the CAT space, we compute cross-attended CATs $\mathbf{x}_{\text{cross, cat}}^L$ using full MCA between all current-level and previous-level CATs:

$$\mathbf{x}_{\text{cross, cat}}^L = \text{LN}(\text{MCA}(\mathbf{x}_{\text{cat}}^{L,t-1}, \text{MLP}(\mathbf{x}_{\text{cat}}^{L-1}))), \quad (3)$$

where $\mathbf{x}_{\text{cat}}^{L-1}$ denotes the final set of CATs from the previous network level. A similar window-based multi-head cross-attention (W-MCA) mechanism is used for capturing relationships between current- and previous-level ITEs, see equation 4. The cross-attended ITEs $\mathbf{x}_{\text{cross}}^L$ are computed as follows:

$$\mathbf{x}_{\text{cross}}^L = \text{LN}(\text{W-MCA}(\mathbf{x}^{L,t-1}, \text{MLP}(\mathbf{x}^{L-1}))), \quad (4)$$

where \mathbf{x}^{L-1} denote the final set of ITEs from the previous network level. Finally, the cross-attended token embeddings are fused using a residual scheme:

$$\begin{aligned}\mathbf{x}_{\text{cat}}^{L,t-1} &= \bar{\mathbf{x}}_{\text{cat}}^{L,t-1} + \mathbf{x}_{\text{cross, cat}}^L \\ \mathbf{x}^{L,t-1} &= \bar{\mathbf{x}}^{L,t-1} + \mathbf{x}_{\text{cross}}^L\end{aligned}\quad (5)$$

Here, $\bar{\mathbf{x}}^{L,t-1}$ and $\bar{\mathbf{x}}_{\text{cat}}^{L,t-1}$ denote ITEs and CATs before fusion. To reduce the complexity of MTVNet, cross-attention is performed only in the first SVHAT layer of every DCHAT block.

4. Experiments

4.1. Experimental setup

Datasets. We use four public MRI datasets and one CT-based dataset to train and evaluate our proposed MTVNet. The Human Connectome Project (HCP) 1200 Subjects dataset [55], the IXI dataset¹, the Brain Tumor Segmentation Challenge (BraTs) 2023 [3–5, 44] and Kirby 21 [35]. These datasets consist of multi-modality image volumes acquired using 1.5T-3T MRI platforms with a volume size of $\leq 320^3$ voxels. The last dataset considered is the Femur Archaeological CT Superresolution (FACTS) dataset [6], which consists of 12 registered 3D volume pairs of archaeological femur bones scanned using clinical-CT and micro-CT. The FACTS dataset features large volumes ($\sim 2000^3$ voxels), enabling us to showcase the benefits of additional contextual information. Two SR tasks are considered using this dataset: In FACTS-Synth, we use downsampled versions of the micro-CT images as the SR model input, while FACTS-Real instead uses the clinical-CT images. The training/test splits for all datasets will be detailed in supplementary material.

Models. To demonstrate the effectiveness of our proposed method, we evaluate the performance of MTVNet against six other volumetric SR models: mDCSRN [15], EDDSR [58], MFER [38], RRDBNet3D [62], SuperFormer [22], and ArSSR [64]. We modify mDCSRN and SuperFormer, which were originally designed to restore images degraded by 3D k-space truncation, a method that simulates LR MRI acquisition [14, 22], by extending these models using the same 3D pixel-shuffle upsampling module used in MTVNet. For EDDSR, MFER, RRDBNet3D and ArSSR, we use the authors' suggested upsampling approach.

Training. We train all models from scratch on each dataset for 100K iterations on a single NVIDIA A100 80GB GPU. For ArSSR, we collate sets of $N = 8000$ randomly sampled HR/LR point pairs from 15 patches for each batch. The remaining models use a batch size of 5 and LR patch size of $32 \times 32 \times 32$, except MTVNet L_2 and L_3 where we use $64 \times 64 \times 64$ and $128 \times 128 \times 128$, respectively. All models are optimized using ADAM [34] with $\beta_1 = 0.9$ and $\beta_2 = 0.999$. We use a multi-step learning rate scheduler, halving the learning rate once after 50k, 70k, 85k, and 95k iterations. The model parameters are optimized using a simple L1 loss metric. HR/LR pairs are generated using volumetric blurring followed by downsampling via linear interpolation. In FACTS-Real, we use the clinical-CT images as LR input but omit blurring since the LR images are already smooth.

Evaluation. For evaluation, we reconstruct all volumetric samples in the test set of each respective dataset using strided aggregation of SR predictions. We tile each SR pre-

¹<https://brain-development.org/ixi-dataset/>

Method	FACTS-Synth Dataset						FACTS-Real Dataset					
	Scale 4×			Scale 3×			Scale 4×			Scale 3×		
	PSNR	SSIM	NRMSE	PSNR	SSIM	NRMSE	PSNR	SSIM	NRMSE	PSNR	SSIM	NRMSE
ArSSR	28.83	.8998	.1779	30.78	.9284	.1459	20.88	.3871	.4881	20.68	.3980	.5767
EDDSR	29.86	.9109	.1620	33.22	.9451	.1104	20.62	.3531	.4815	19.84	.3499	.5223
MFER	29.48	.9094	.1646	32.50	.9420	.1179	21.58	.4708	.4080	21.64	.4671	.4096
mDCSRN	29.77	.9099	.1624	33.23	.9460	.1090	21.31	.4078	.4765	21.37	.4259	.4922
SuperFormer	30.46	.9175	.1481	33.47	.9480	.1055	20.93	.3491	.4846	21.40	.4038	.4463
RRDBNet3D	29.78	.9120	.1584	33.21	.9442	.1093	21.64	.4670	.4022	21.91	.4775	.4019
MTVNet	31.57	.9303	.1313	33.91	.9502	.1020	21.52	.4576	.4061	21.74	.4633	.4051
HCP 1200 Dataset												
Method	Scale 4×			Scale 2×			Scale 4×			Scale 2×		
	PSNR	SSIM	NRMSE	PSNR	SSIM	NRMSE	PSNR	SSIM	NRMSE	PSNR	SSIM	NRMSE
	27.90	.8118	.2810	35.54	.9372	.1212	24.22	.7204	.3060	30.32	.9152	.1560
ArSSR	27.90	.8118	.2810	35.54	.9372	.1212	24.22	.7204	.3060	30.32	.9152	.1560
EDDSR	30.12	.8335	.2174	35.19	.9317	.1274	25.22	.7394	.2597	33.45	.9447	.1101
MFER	33.40	.8933	.1484	37.24	.9498	.1011	25.23	.7611	.2576	35.67	.9622	.0865
mDCSRN	33.46	.8941	.1470	37.18	.9493	.1017	29.50	.8558	.1622	35.66	.9619	.0863
SuperFormer	33.70	.8982	.1430	36.65	.9441	.1080	29.89	.8679	.1545	35.00	.9575	.0925
RRDBNet3D	34.31	.9092	.1331	37.70	.9533	.0959	30.27	.8793	.1488	36.92	.9697	.0755
MTVNet	34.04	.9046	.1374	37.53	.9520	.0978	30.16	.8754	.1502	36.38	.9668	.0799
BraTS 2023 Dataset												
Method	Scale 4×			Scale 2×			Scale 4×			Scale 2×		
	PSNR	SSIM	NRMSE	PSNR	SSIM	NRMSE	PSNR	SSIM	NRMSE	PSNR	SSIM	NRMSE
	22.96	.3182	.4437	36.67	.9691	.1079	31.82	.8632	.2775	43.94	.9860	.0705
ArSSR	22.96	.3182	.4437	36.67	.9691	.1079	31.82	.8632	.2775	43.94	.9860	.0705
EDDSR	32.66	.9169	.1686	38.29	.9766	.0916	33.51	.8946	.2244	44.42	.9874	.0693
MFER	34.76	.9430	.1309	41.88	.9867	.0614	35.68	.9307	.1719	51.51	.9970	.0309
mDCSRN	34.76	.9431	.1308	41.88	.9865	.0614	35.26	.9255	.1806	50.64	.9962	.0345
SuperFormer	34.60	.9400	.1333	40.46	.9831	.0716	35.85	.9341	.1675	48.14	.9936	.0453
RRDBNet3D	35.20	.9486	.1242	43.76	.9894	.0501	36.27	.9376	.1598	56.36	.9988	.0175
MTVNet	35.16	.9477	.1250	42.71	.9880	.0560	35.97	.9355	.1654	53.60	.9977	.0247
Kirby 21 Dataset												

Table 1. Quantitative comparison of state-of-the-art volumetric SR models on datasets FACTS-Synth, FACTS-Real, HCP 1200, IXI, BraTS 2023, and Kirby 21. The best performance metrics PSNR ↑ / SSIM ↑ / NRMSE ↓ are highlighted in red, and the second best in blue.

dition using an overlap of $4 \times s$ voxels where s is the upscaling factor and smooth the overlapping prediction areas using a Hanning window. The performance metrics Peak-Signal-to-Noise Ratio (PSNR), Structural Similarity Index Measure (SSIM), and Normalized Root Mean Square Error (NRMSE) are computed slice-wise in the axial direction and averaged over all samples in each dataset, ignoring any slices where the foreground occupies less than 25% of the voxels.

4.2. Implementation details

All MTVNet configurations use a learning rate of $2e-4$ with no weight decay. For the brain MRI datasets (HCP 1200, IXI, BraTs 2023, and Kirby 21), we apply MTVNet L_2 with two levels featuring two DCHAT blocks in the first level and three DCHAT blocks in the second level, each

with six SVHAT layers. For the FACTS dataset, we use MTVNet L_3 consisting of a third level with one DCHAT block on top of L_2 . In all configurations of MTVNet, the number of shallow features and intermediate features is set to $C_{emb} = 128$, and the number of compressed features in each skip-connection is set to $C_{skip} = 64$. In MTVNet L_3 we use patch sizes $p_3 = 8$, $p_2 = 4$ and $p_1 = 2$ for volumetric patch embedding at each subsequent network level while in MTVNet L_2 , patch sizes are set to $p_2 = 4$ and $p_1 = 2$. The attention window size and the size of the CAT space for each window are set to $M = 8$ and $c = 4$, respectively. To reduce memory usage during upsampling, we halve the number of features channels in MTVNet, mDCSRN, SuperFormer, and RRDBNet3D before upsampling.

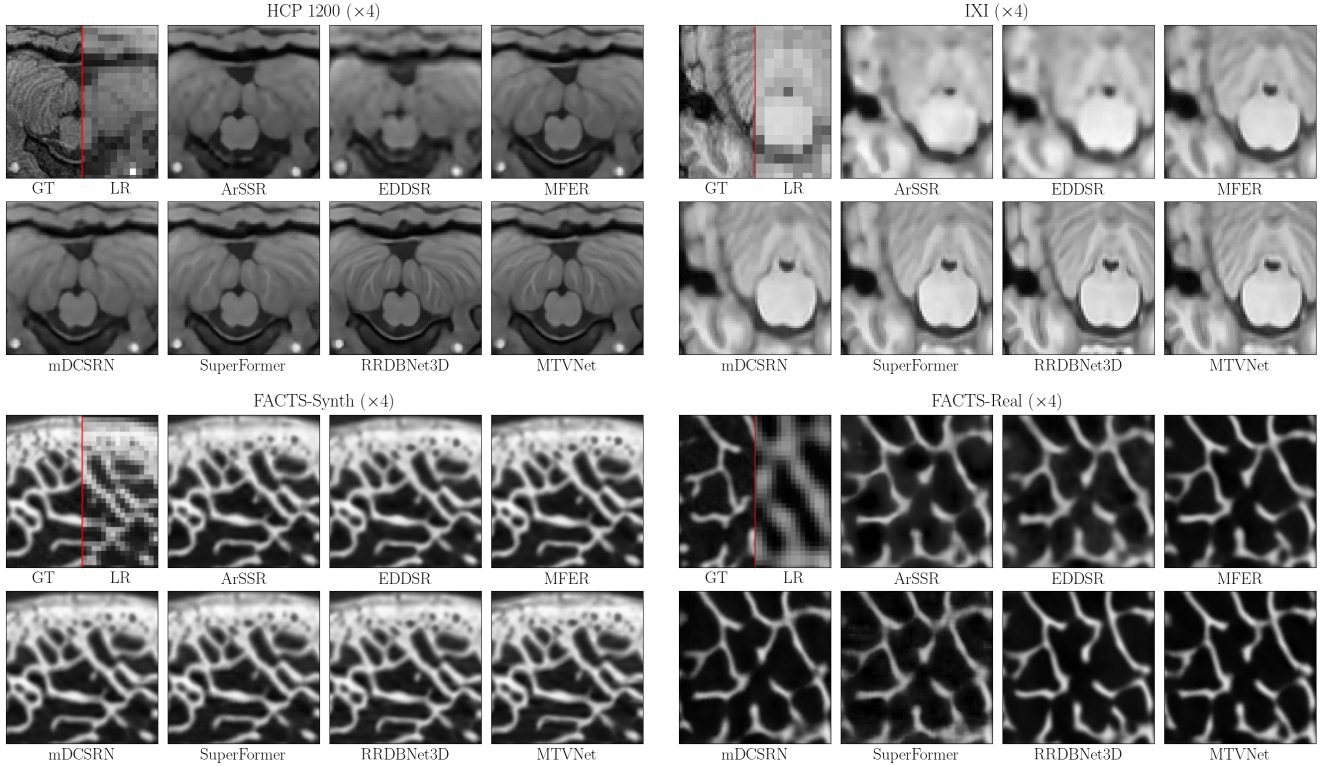


Figure 4. Visual comparisons of SR model outputs from the datasets HCP 1200, IXI, FACTS-Synth, and FACTS-Real using $4\times$ upscaling. The ground truth (GT) and LR input images are shown side-by-side in the top-left separated by the red line.

4.3. Quantitative results

Tab. 1 shows a quantitative comparison between MTVNet and six other SOTA volumetric SR models ArSSR [64], EDDSR [58], MFER [38], mDCSRN [15], SuperFormer [22], and RRDBNet3D [62]. In the brain MRI benchmark datasets HCP 1200, IXI, BraTs 2023, and Kirby 21 our MTVNet achieves second best performance across all scales. Contradicting the findings of Forigua et al. [22], we observe the purely CNN-based method RRDBNet3D achieving better performance metrics than the transformer-based SuperFormer and our method. We reason that the advantage of RRDBNet3D may be due to local image dependencies being predominant in these datasets, limiting the benefit of the broader receptive field offered by ViTs. Still, our MTVNet achieves only slightly lower performance than RRDBNet3D while there is a greater performance gap between our method and SuperFormer, especially in $2\times$ upscaling.

In the FACTS dataset, where we can leverage the multi-contextual architecture of our proposed method, we observe several new trends: In FACTS-Synth, our proposed MTVNet outperforms all other methods by a significant margin at all scales. Compared with SuperFormer, MTVNet improves PSNR scores by $0.44\text{dB}\sim1.11\text{dB}$ and

by $0.70\text{dB}\sim1.79\text{dB}$ when compared with RRDBNet3D. These improvements illustrate that additional contextual information enables significant SR performance gains in high-resolution volumetric images. In FACTS-Real where the clinical-CT images are used as LR model input, we observe CNN-based methods RRDBNet3D, MFER, and our MTVNet achieve the best results. We hypothesize that this discrepancy in performance results from the domain shift between micro-CT and clinical-CT, which largely deprives the clinical-CT images of long-range image dependencies. The trabecular structure in the clinical-CT images is largely indistinguishable, whereas the LR micro-CT images show more distinct repeatable patterns that could offer more valuable contextual information. Therefore, we surmise that the performance gains of incorporating additional long-range information in MTVNet diminishes for this SR task.

4.4. Qualitative results

Fig. 4 shows a visual comparison of SR predictions on scale $4\times$ for HCP 1200, IXI, FACTS-Synth, and FACTS-Real. We find that MTVNet produces faithful reconstructions of structures and patterns across all datasets. Compared with ArSSR, EDDSR, MFER, mDCSRN, and SuperFormer, our MTVNet produces notably sharper features while producing similar results as RRDBNet3D. In the

Method	Cyclic shift	CAT	Multi context	PSNR/SSIM/NRMSE BraTS 2023 ($\times 4$)
SW-MSA	✓	✗	✗	35.00 / .9460 / .1273
MSA w. CAT	✗	✓	✗	35.02 / .9463 / .1269
SW-MSA w. CAT	✓	✓	✗	35.05 / .9467 / .1265
MTVNet	✓	✓	✓	<u>35.16</u> / <u>.9477</u> / <u>.1250</u>

Table 2. Ablation on the proposed features of MTVNet. The best performance metrics PSNR/SSIM/NRMSE are underlined.

Brain MRI datasets HCP 1200 and IXI, we find that many methods struggle to reconstruct anatomical details while RRDBNet3D and our MTVNet produce the clearest results. In FACTS-Synth, we find that other models tend to produce unnaturally blurred textures, whereas our proposed MTVNet suffers much less from these artifacts.

4.5. Ablation experiments

We study the effect of our proposed features of MTVNet, including the addition of CATs, shifted window hierarchical attention, and multi-contextual network levels. Tab. 2 shows a quantitative comparison on the BraTS 2023 dataset using $\times 4$ upscaling. Replacing the SW-MSA procedure [41] with CAT-based hierarchical attention results in slight performance gains across all metrics, though only marginally compared to the gains seen in FasterViT [28]. Since CATs contain compressed feature summaries of each attention window, we hypothesize that this compression process discards most of the pixel-level information essential for SR. These details are less critical in image classification, hence why CATs have been observed to result in higher performance gains in this domain [28]. Incorporating our modified SW-MSA mechanism with CATs improves the receptive field and positively impacts performance. Finally, adding multi-contextual information in MTVNet yields the largest relative improvement, increasing PSNR by 0.11dB~0.16dB over other configurations. Notably, even with the relatively small volumetric samples ($\leq 240^3$ voxels) in BraTS 2023, MTVNet benefits from multi-contextual information. These results highlight the value of additional contextual information, even in small-scale volumetric SR.

4.6. Memory footprint of MTVNet

Fig. 5 shows the memory footprint required by SuperFormer, RRDBNet3D, and MTVNet using different volumetric input resolutions. Using a single level, MTVNet L_1 requires less memory than SuperFormer and RRDBNet3D. Furthermore, provided the prediction area is fixed to 32^3 , adding more network levels to MTVNet allows processing volumetric input sizes far exceeding the capabilities of other volumetric SR architectures.

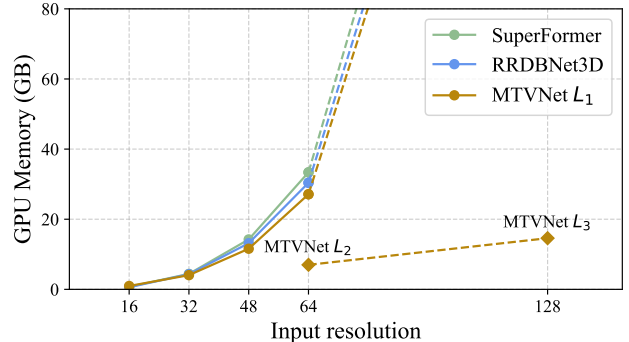


Figure 5. GPU Memory usage of SuperFormer, RRDBNet3D, and MTVNet using a single 3D patch at resolutions 16^3 , 32^3 , 48^3 , and 64^3 . Adding contextual levels to MTVNet enables increasing resolution to 128^3 and beyond without exceeding GPU memory.

5. Conclusion

In this work, we present MTVNet, a transformer-based approach for volumetric SR tailored for high-resolution 3D data. To overcome the challenge of limited contextual information in volumetric SR, we propose a multi-contextual network structure with a coarse-to-fine feature extraction and tokenization scheme. This approach reduces the number of tokens needed to cover large volumetric regions, allowing our model to process significantly larger input sizes than competing methods. To enhance long-range information exchange in the expanded input volume, we implement a novel shifting volumetric hierarchical attention transformer (SVHAT) layer inspired by FasterViT [28] and SwinV2 [42] that employs a combination of full and window-based attention to capture both global and local image dependencies. We evaluate the performance of MTVNet against other volumetric SR approaches across several data domains, including brain MRI data and high-resolution CT data. Based on extensive experiments, we make several conclusions: In contradiction with the current research trends in 2D SR, we observe CNN-based models outperform transformer-based models in certain data domains. The effectiveness of CNN-based SR models is especially pronounced in lower-resolution 3D samples where the larger receptive field of transformers cannot be leveraged as effectively. Nevertheless, our proposed MTVNet with extra contextual processing layers outperforms all other models given high-resolution 3D data with meaningful long-range image dependencies.

We surmise that our multi-contextual approach for volumetric image processing could be greatly beneficial for other vision applications such as segmentation, classification, and recognition in volumetric images.

References

[1] Andrew P. Aitken, Christian Ledig, Lucas Theis, Jose Caballero, Zehan Wang, and Wenzhe Shi. Checkerboard artifact free sub-pixel convolution: A note on sub-pixel convolution, resize convolution and convolution resize. *ArXiv*, abs/1707.02937, 2017. 4

[2] Jimmy Ba, Jamie Kiros, and Geoffrey Hinton. Layer normalization. *ArXiv e-prints*, 2016. 5

[3] Ujjwal Baid, Satyam Ghodasara, Suyash Mohan, M Bilello, E Calabrese, E Colak, K Farahani, J Kalpathy-Cramer, FC Kitamura, S Pati, et al. The rsna-asnr-miccai brats 2021 benchmark on brain tumor segmentation and radiogenomic classification. *arXiv* 2021. *arXiv preprint arXiv:2107.02314*, 2021. 5, 1

[4] Spyridon Bakas, Hamed Akbari, Aristeidis Sotiras, Michel Bilello, Martin Rozycki, Justin Kirby, John Freymann, Keyvan Farahani, and Christos Davatzikos. Segmentation labels and radiomic features for the pre-operative scans of the tcga-lgg collection. *The cancer imaging archive*, 286, 2017.

[5] Spyridon Bakas, Hamed Akbari, Aristeidis Sotiras, Michel Bilello, Martin Rozycki, Justin S Kirby, John B Freymann, Keyvan Farahani, and Christos Davatzikos. Advancing the cancer genome atlas glioma mri collections with expert segmentation labels and radiomic features. *Scientific data*, 4(1): 1–13, 2017. 5, 1

[6] Sophia W. Bardenfleth, Vedrana A. Dahl, Chiara Villa, Galateia Kazakia, and Anders B. Dahl. Superresolution of real-world multiscale bone ct verified with clinical bone measures. In *Medical Image Understanding and Analysis*, pages 160–173, Cham, 2024. Springer Nature Switzerland. 5, 1

[7] Hu Cao, Yueyue Wang, Joy Chen, Dongsheng Jiang, Xiaopeng Zhang, Qi Tian, and Manning Wang. Swin-Unet: Unet-like pure transformer for medical image segmentation. In *European conference on computer vision*, pages 205–218. Springer, 2022. 2

[8] Nicolas Carion, Francisco Massa, Gabriel Synnaeve, Nicolas Usunier, Alexander Kirillov, and Sergey Zagoruyko. End-to-end object detection with transformers. In *European conference on computer vision*, pages 213–229. Springer, 2020. 2

[9] Chun-Fu Chen, Quanfu Fan, and Rameswar Panda. Crossvit: Cross-attention multi-scale vision transformer for image classification. In *Proceedings of the IEEE/CVF international conference on computer vision*, pages 357–366, 2021. 2

[10] Jieneng Chen, Yongyi Lu, Qihang Yu, Xiangde Luo, Ehsan Adeli, Yan Wang, Le Lu, Alan Loddon Yuille, and Yuyin Zhou. Transunet: Transformers make strong encoders for medical image segmentation. *arXiv preprint arXiv:2102.04306*, 2021. 2

[11] Xiangyu Chen, Xintao Wang, Wenlong Zhang, Xiangtao Kong, Yu Qiao, Jiantao Zhou, and Chao Dong. Hat: Hybrid attention transformer for image restoration. *arXiv preprint arXiv:2309.05239*, 2023. 2

[12] Xiangyu Chen, Xintao Wang, Jiantao Zhou, Yu Qiao, and Chao Dong. Activating more pixels in image super-resolution transformer. In *Proceedings of the IEEE/CVF Conference on Computer Vision and Pattern Recognition (CVPR)*, pages 22367–22377, 2023. 1, 2

[13] Yuhua Chen, Feng Shi, Anthony G Christodoulou, Yibin Xie, Zhengwei Zhou, and Debiao Li. Efficient and accurate mri super-resolution using a generative adversarial network and 3d multi-level densely connected network. In *International conference on medical image computing and computer-assisted intervention*, pages 91–99. Springer, 2018. 1, 2

[14] Yuhua Chen, Yibin Xie, Zhengwei Zhou, Feng Shi, Anthony Christodoulou, and Debiao Li. Brain MRI super resolution using 3D deep densely connected neural networks. In *2018 IEEE 15th international symposium on biomedical imaging (ISBI 2018)*, pages 739–742. IEEE, 2018. 2, 5

[15] Yuhua Chen, Anthony G. Christodoulou, Zhengwei Zhou, Feng Shi, Yibin Xie, and Debiao Li. MRI super-resolution with GAN and 3D multi-level densenet: Smaller, faster, and better. *arXiv preprint arXiv:2003.01217*, 2020. 1, 2, 5, 7

[16] Shu-Chuan Chu, Zhi-Chao Dou, Jeng-Shyang Pan, Shaowei Weng, and Junbao Li. HMAnet: Hybrid multi-axis aggregation network for image super-resolution. In *Proceedings of the IEEE/CVF Conference on Computer Vision and Pattern Recognition (CVPR) Workshops*, pages 6257–6266, 2024. 1, 2

[17] Marcos V. Conde, Ui-Jin Choi, Maxime Burchi, and Radu Timofte. Swin2sr: Swin2 transformer for compressed image super-resolution and restoration. In *European Conference on Computer Vision*, pages 669–687. Springer, 2023. 2

[18] Chao Dong, Chen Change Loy, Kaiming He, and Xiaoou Tang. Image super-resolution using deep convolutional networks. *IEEE Transactions on Pattern Analysis and Machine Intelligence*, 38(2):295–307, 2016. 2

[19] Chao Dong, Chen Change Loy, and Xiaoou Tang. Accelerating the super-resolution convolutional neural network. In *Computer Vision – ECCV 2016*, pages 391–407. Springer, 2016. 2

[20] Alexey Dosovitskiy, Lucas Beyer, Alexander Kolesnikov, Dirk Weissenborn, Xiaohua Zhai, Thomas Unterthiner, Mostafa Dehghani, Matthias Minderer, Georg Heigold, Sylvain Gelly, Jakob Uszkoreit, and Neil Houlsby. An image is worth 16x16 words: Transformers for image recognition at scale. *ArXiv*, abs/2010.11929, 2021. 1, 2

[21] Jinglong Du, Lulu Wang, Yulu Liu, Zexun Zhou, Zhongshi He, and Yuanyuan Jia. Brain MRI super-resolution using 3D dilated convolutional encoder–decoder network. *IEEE Access*, 8:18938–18950, 2020. 2

[22] Cristian Forigua, Maria Escobar, and Pablo Arbelaez. SuperFormer: Volumetric transformer architectures for MRI super-resolution. In *International Workshop on Simulation and Synthesis in Medical Imaging*, pages 132–141. Springer, 2022. 1, 2, 3, 5, 7

[23] Yunhe Gao, Mu Zhou, Ding Liu, and Dimitris N. Metaxas. A multi-scale transformer for medical image segmentation: Architectures, model efficiency, and benchmarks. *arXiv preprint arXiv:2203.00131*, 2022. 2

[24] Ziteng Gao, Limin Wang, Bing Han, and Sheng Guo. Adamixer: A fast-converging query-based object detector.

2022 IEEE/CVF Conference on Computer Vision and Pattern Recognition (CVPR), pages 5354–5363, 2022. 2

[25] Rongjun Ge, Guanyu Yang, Chenchu Xu, Yang Chen, Limin Luo, and Shuo Li. Stereo-correlation and noise-distribution aware ResVoxGAN for dense slices reconstruction and noise reduction in thick low-dose CT. In *Medical Image Computing and Computer Assisted Intervention–MICCAI 2019: 22nd International Conference, Shenzhen, China, October 13–17, 2019, Proceedings, Part VI 22*, pages 328–338. Springer, 2019. 3

[26] Jinjin Gu and Chao Dong. Interpreting super-resolution networks with local attribution maps. In *Proceedings of the IEEE/CVF Conference on Computer Vision and Pattern Recognition (CVPR)*, pages 9199–9208, 2021. 2

[27] Ali Hatamizadeh, Vishwesh Nath, Yucheng Tang, Dong Yang, Holger R. Roth, and Daguang Xu. Swin unetr: Swin transformers for semantic segmentation of brain tumors in mri images. In *Brainlesion: Glioma, Multiple Sclerosis, Stroke and Traumatic Brain Injuries*, pages 272–284, Cham, 2022. Springer International Publishing. 2

[28] Ali Hatamizadeh, Greg Heinrich, Hongxu Yin, Andrew Tao, Jose M Alvarez, Jan Kautz, and Pavlo Molchanov. FasterViT: Fast vision transformers with hierarchical attention. *arXiv preprint arXiv:2306.06189*, 2023. 2, 4, 8, 1

[29] Chih-Chung Hsu, Chia-Ming Lee, and Yi-Shiuan Chou. Drct: Saving image super-resolution away from information bottleneck. In *Proceedings of the IEEE/CVF Conference on Computer Vision and Pattern Recognition (CVPR) Workshops*, pages 6133–6142, 2024. 1, 2, 4

[30] Gao Huang, Zhuang Liu, Laurens Van Der Maaten, and Kilian Q. Weinberger. Densely connected convolutional networks. In *2017 IEEE Conference on Computer Vision and Pattern Recognition (CVPR)*, pages 2261–2269, 2017. 2

[31] Zexin Ji, Beiji Zou, Xiaoyan Kui, Jun Liu, Wei Zhao, Chengzhang Zhu, Peishan Dai, and Yulan Dai. Deep learning-based magnetic resonance image super-resolution: a survey. *Neural Computing and Applications*, 36(21):12725–12752, 2024. 3

[32] Zexin Ji, Beiji Zou, Xiaoyan Kui, Jun Liu, Wei Zhao, Chengzhang Zhu, Peishan Dai, and Yulan Dai. Deep learning-based magnetic resonance image super-resolution: a survey. *Neural Computing and Applications*, pages 1–28, 2024. 1

[33] Xuhao Jiang, Yifei Xu, Pingping Wei, and Zhuming Zhou. Ct image super resolution based on improved srgan. In *2020 5th International Conference on Computer and Communication Systems (ICCCS)*, pages 363–367. IEEE, 2020. 1

[34] Diederik P. Kingma and Jimmy Ba. Adam: A method for stochastic optimization. *CoRR*, abs/1412.6980, 2014. 5

[35] Bennett A Landman, Alan J Huang, Aliya Gifford, Deepa S Vikram, Issel Anne L Lim, Jonathan AD Farrell, John A Bogovic, Jun Hua, Min Chen, Samson Jarso, et al. Multi-parametric neuroimaging reproducibility: a 3-t resource study. *Neuroimage*, 54(4):2854–2866, 2011. 5, 1

[36] Christian Ledig, Lucas Theis, Ferenc Huszár, Jose Caballero, Andrew P. Aitken, Alykhan Tejani, Johannes Totz, Zehan Wang, and Wenzhe Shi. Photo-realistic single image super-resolution using a generative adversarial network. 2017 IEEE Conference on Computer Vision and Pattern Recognition (CVPR), pages 105–114, 2016. 2

[37] Guangyuan Li, Lei Zhao, Jiakai Sun, Zehua Lan, Zhanjie Zhang, Jiafu Chen, Zhijie Lin, Huaizhong Lin, and Wei Xing. Rethinking multi-contrast mri super-resolution: Rectangle-window cross-attention transformer and arbitrary-scale upsampling. In *Proceedings of the IEEE/CVF International Conference on Computer Vision (ICCV)*, pages 21230–21240, 2023. 3

[38] Hongbi Li, Yuanyuan Jia, Huazheng Zhu, Baoru Han, Jinglong Du, and Yanbing Liu. Multi-level feature extraction and reconstruction for 3d mri image super-resolution. *Computers in Biology and Medicine*, 171:108151, 2024. 2, 5, 7

[39] Jingyun Liang, Jiezheng Cao, Guolei Sun, Kai Zhang, Luc Van Gool, and Radu Timofte. Swinir: Image restoration using swin transformer. In *Proceedings of the IEEE/CVF international conference on computer vision*, pages 1833–1844, 2021. 1, 2, 3

[40] Bee Lim, Sanghyun Son, Heewon Kim, Seungjun Nah, and Kyoung Mu Lee. Enhanced deep residual networks for single image super-resolution. In *Proceedings of the IEEE Conference on Computer Vision and Pattern Recognition (CVPR) Workshops*, 2017. 2

[41] Ze Liu, Yutong Lin, Yue Cao, Han Hu, Yixuan Wei, Zheng Zhang, Stephen Lin, and Baining Guo. Swin transformer: Hierarchical vision transformer using shifted windows. 2021 IEEE/CVF International Conference on Computer Vision (ICCV), pages 9992–10002, 2021. 1, 2, 3, 8

[42] Ze Liu, Han Hu, Yutong Lin, Zhuliang Yao, Zhenda Xie, Yixuan Wei, Jia Ning, Yue Cao, Zheng Zhang, Li Dong, Furu Wei, and Baining Guo. Swin transformer v2: Scaling up capacity and resolution. In *International Conference on Computer Vision and Pattern Recognition (CVPR)*, 2022. 2, 4, 5, 8, 1

[43] Wei Lu, Zhijin Song, and Jinghui Chu. A novel 3d medical image super-resolution method based on densely connected network. *Biomedical Signal Processing and Control*, 62:102120, 2020. 2

[44] Bjoern H Menze, Andras Jakab, Stefan Bauer, Jayashree Kalpathy-Cramer, Keyvan Farahani, Justin Kirby, Yuliya Burren, Nicole Porz, Johannes Slotboom, Roland Wiest, et al. The multimodal brain tumor image segmentation benchmark (brats). *IEEE transactions on medical imaging*, 34(10):1993–2024, 2014. 5, 1

[45] Ozan Oktay, Wenjia Bai, Matthew Lee, Ricardo Guerrero, Konstantinos Kamnitsas, Jose Caballero, Antonio de Marvao, Stuart Cook, Declan O'Regan, and Daniel Rueckert. Multi-input cardiac image super-resolution using convolutional neural networks. In *Medical Image Computing and Computer-Assisted Intervention-MICCAI 2016: 19th International Conference, Athens, Greece, October 17–21, 2016, Proceedings, Part III 19*, pages 246–254. Springer, 2016. 1

[46] Chi-Hieu Pham, Aurélien Ducournau, Ronan Fablet, and François Rousseau. Brain MRI super-resolution using deep 3d convolutional networks. In *2017 IEEE 14th International Symposium on Biomedical Imaging (ISBI 2017)*, pages 197–200, 2017. 2

[47] Chi-Hieu Pham, Carlos Tor-Díez, Hélène Meunier, Nathalie Bednarek, Ronan Fablet, Nicolas Passat, and François Rousseau. Multiscale brain mri super-resolution using deep 3d convolutional networks. *Computerized Medical Imaging and Graphics*, 77:101647, 2019. [1](#), [2](#)

[48] Byungseok Roh, Jaewoong Shin, Wuhyun Shin, and Sae-hoon Kim. Sparse detr: Efficient end-to-end object detection with learnable sparsity. *ArXiv*, abs/2111.14330, 2021. [2](#)

[49] Irina Sánchez and Verónica Vilaplana. Brain MRI super-resolution using 3d generative adversarial networks. *ArXiv*, abs/1812.11440, 2018. [2](#)

[50] Tahira Shehzadi, Khurram Azeem Hashmi, Didier Stricker, and Muhammad Zeshan Afzal. Object detection with transformers: A review. *ArXiv*, abs/2306.04670, 2023. [2](#)

[51] Wenzhe Shi, Jose Caballero, Ferenc Huszár, Johannes Totz, Andrew P. Aitken, Rob Bishop, Daniel Rueckert, and Zehan Wang. Real-time single image and video super-resolution using an efficient sub-pixel convolutional neural network. *2016 IEEE Conference on Computer Vision and Pattern Recognition (CVPR)*, pages 1874–1883, 2016. [4](#)

[52] Liyao Song, Quan Wang, Ting Liu, Haiwei Li, Jiancun Fan, Jian Yang, and Bingliang Hu. Deep robust residual network for super-resolution of 2d fetal brain mri. *Scientific reports*, 12(1):406, 2022. [1](#)

[53] Mukund Sundararajan, Ankur Taly, and Qiqi Yan. Axiomatic attribution for deep networks. In *International conference on machine learning*, pages 3319–3328. PMLR, 2017. [2](#)

[54] Tong Tong, Gen Li, Xiejie Liu, and Qinquan Gao. Image super-resolution using dense skip connections. In *2017 IEEE International Conference on Computer Vision (ICCV)*, pages 4809–4817, 2017. [2](#)

[55] David C Van Essen, Stephen M Smith, Deanna M Barch, Timothy EJ Behrens, Essa Yacoub, Kamil Ugurbil, Wu-Minn HCP Consortium, et al. The wu-minn human connectome project: an overview. *Neuroimage*, 80:62–79, 2013. [5](#), [1](#)

[56] Ashish Vaswani, Noam M. Shazeer, Niki Parmar, Jakob Uszkoreit, Llion Jones, Aidan N. Gomez, Łukasz Kaiser, and Illia Polosukhin. Attention is all you need. In *Neural Information Processing Systems*, 2017. [4](#), [5](#)

[57] CL Walsh, P Tafforeau, WL Wagner, DJ Jafree, A Bellier, C Werlein, MP Kühnel, E Boller, S Walker-Samuel, JL Rober tus, et al. Imaging intact human organs with local resolution of cellular structures using hierarchical phase-contrast tomography. *Nature methods*, 18(12):1532–1541, 2021. [1](#)

[58] Lulu Wang, Jinglong Du, Ali Gholipour, Huazheng Zhu, Zhongshi He, and Yuanyuan Jia. 3d dense convolutional neural network for fast and accurate single mr image super-resolution. *Computerized Medical Imaging and Graphics*, 93:101973, 2021. [2](#), [5](#), [7](#)

[59] Lulu Wang, Huazheng Zhu, Zhongshi He, Yuanyuan Jia, and Jinglong Du. Adjacent slices feature transformer network for single anisotropic 3d brain mri image super-resolution. *Biomedical Signal Processing and Control*, 72: 103339, 2022. [3](#)

[60] Shanshan Wang, Zhenghang Su, Leslie Ying, Xi Peng, Shun Zhu, Feng Liang, Dagan Feng, and Dong Liang. Accelerating magnetic resonance imaging via deep learning. In *2016 IEEE 13th international symposium on biomedical imaging (ISBI)*, pages 514–517. IEEE, 2016. [1](#)

[61] Wenzuan Wang, Chen Chen, Meng Ding, Hong Yu, Sen Zha, and Jiangyun Li. Transsts: Multimodal brain tumor segmentation using transformer. In *Medical Image Computing and Computer Assisted Intervention – MICCAI 2021*, pages 109–119, Cham, 2021. Springer International Publishing. [2](#)

[62] Xintao Wang, Ke Yu, Shixiang Wu, Jinjin Gu, Yihao Liu, Chao Dong, Yu Qiao, and Chen Change Loy. ESRGAN: Enhanced super-resolution generative adversarial networks. In *Computer Vision – ECCV 2018 Workshops*, pages 63–79. Springer, 2019. [2](#), [5](#), [7](#)

[63] Eckhard Wehrse, Laura Klein, Lukas Thomas Rotkopf, Wolfram Stiller, M Finke, Gernot G Echner, Christin Glowa, Sarah Heinze, Christian Herbert Ziener, Heinz Peter Schlemmer, et al. Ultrahigh resolution whole body photon counting computed tomography as a novel versatile tool for translational research from mouse to man. *Zeitschrift für Medizinische Physik*, 33(2):155–167, 2023. [1](#)

[64] Qing Wu, Yuwei Li, Yawen Sun, Yan Zhou, Hongjiang Wei, Jingyi Yu, and Yuyao Zhang. An arbitrary scale super-resolution approach for 3d mr images via implicit neural representation. *IEEE Journal of Biomedical and Health Informatics*, 27(2):1004–1015, 2023. [2](#), [3](#), [5](#), [7](#)

[65] Hao Xia, Nian Cai, Huiheng Wang, Yadong Mao, Han Wang, Jian Li, and Ping Wang. Brain mr image super-resolution via a deep convolutional neural network with multi-unit up-sampling learning. *Signal, Image and Video Processing*, 15: 931–939, 2021. [1](#)

[66] Wanqi Zhang, Lulu Wang, Wei Chen, Yuanyuan Jia, Zhongshi He, and Jinglong Du. 3d cross-scale feature transformer network for brain mr image super-resolution. In *ICASSP 2022 - 2022 IEEE International Conference on Acoustics, Speech and Signal Processing (ICASSP)*, pages 1356–1360, 2022. [3](#)

[67] Yulun Zhang, Kunpeng Li, Kai Li, Lichen Wang, Bineng Zhong, and Yun Fu. Image super-resolution using very deep residual channel attention networks. In *Computer Vision – ECCV 2018*, pages 294–310, Cham, 2018. Springer International Publishing. [2](#), [3](#)

[68] Jin Zhu, Chuan Tan, Junwei Yang, Guang Yang, and Pietro Lio’. Arbitrary scale super-resolution for medical images. *International Journal of Neural Systems*, 31(10):2150037, 2021. PMID: 34304719. [3](#)

MTVNet: Mapping using Transformers for Volumes – Network for Super-Resolution with Long-Range Interactions

Supplementary Material

6. Details of SVHAT layer

Fig. 6 provides an overview of our proposed shifting volumetric hierarchical attention transformer (SVHAT) layer. Our SVHAT captures global and local token dependencies using separate attention branches for CATs and ITEs. The CAT attention branch (shown in red) follows the attention procedure of FasterViT [28], whereas the ITE branch (shown in blue) follows the approach of SwinV2 [42]. Before computing attention in each branch, SVHAT uses full multi-head cross-attention (MCA) for computing attention between CATs extracted from different network levels in MTVNet. Similarly, windowed multi-head cross-attention (W-MCA) is used for computing attention between ITEs from different network levels.

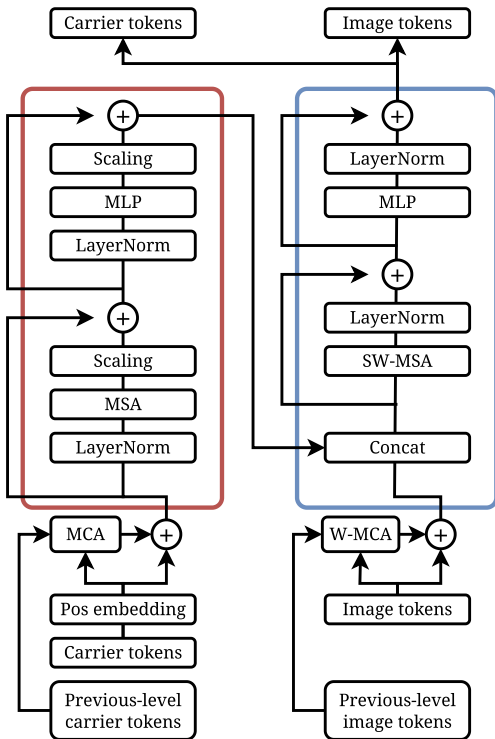


Figure 6. Overview of SVHAT featuring attention branches for CATs (red) and ITEs (blue). We use MCA and W-MCA to merge tokens from previous network levels before computing attention in each branch.

7. Datasets

Human Connectome Project (HCP) 1200

The HCP 1200 Subjects Data Release [55] includes structural MRI scans from 1113 healthy subjects acquired using a 3T scanning platform. We use the T1-weighted images which feature an isotropic resolution of 0.7 mm and a volume size of $320 \times 320 \times 256$ voxels. Following the approach in [15, 22], the dataset is split into 780 subjects for training, and 111 subjects each for validation, evaluation, and testing. Performance evaluation is performed using the 111 subjects in the test set.

Information eXtraction from Images (IXI)

The IXI dataset contains multi-modality MRI data (PD-, T1- and T2-weighted images) collected from a total of 600 healthy subjects scanned using one 3T, and two 1.5T platforms. We use all 581 T1-weighted images of IXI, of which 507 scans feature a resolution of $0.9375 \times 0.9375 \times 1.2$ mm and a volume size of $256 \times 256 \times 150$ voxels, and the remaining 74 scans feature a resolution of $0.93749 \times 0.9375 \times 1.2$ mm and a volume size of $256 \times 256 \times 146$ voxels. The dataset is split into 500 subjects for training, 6 for validation, and 75 for testing. Performance evaluation is performed using the 75 subjects in the test set.

Brain Tumor Segmentation Challenge (BraTS) 2023

For BraTS 2023, we use the T1-weighted structural MRI images of the Adult Glioma segmentation challenge [3–5, 44]. This subset contains a total of 1,470 scans collected from glioma patients. The images are skull-stripped and standardized to an isotropic resolution of 1 mm and a volume size of $240 \times 240 \times 155$ voxels. We use the dataset split provided by the Adult Glioma segmentation challenge, which allocates 1,251 subjects for training and 219 for validation. Performance evaluation is performed using the 219 subjects in the validation set.

Kirby 21

The Kirby 21 dataset [35] includes multi-modality MRI images acquired from healthy individuals with no history of neurological conditions. We use all 42 T2-weighted images of Kirby 21 which feature a resolution of $1 \times 0.9375 \times 0.9375$ mm and a volume size of $180 \times 256 \times 256$ voxels. The dataset is split into 37 images for training (KKI-06 to KKI-42) and 5 for testing (KKI-01 to KKI-5). Performance evaluation is performed using the 5 subjects in the test set.

Femur Archaeological CT Superresolution (FACTS)

The FACTS dataset consists of 12 archaeological proximal femurs scanned using clinical-CT and micro-CT platforms [6]. The clinical-CT and micro-CT scans feature a resolu-

tion of $0.21 \times 0.21 \times 0.4$ mm and $58 \times 58 \times 58 \mu\text{m}$, respectively. The clinical-CT volumes are registered and linearly interpolated to match the volume sizes of the micro-CT images. The dataset is split into 10 images for training and 2 images (f_002 and f_138) for testing and subsequent performance evaluation.

8. Visual comparisons using LAM

We investigate how effectively volumetric SR models utilize the surrounding image context when computing SR predictions. To this end, we employ the LAM attribution method [26], which is a modification of the integrated gradient method [53] designed to investigate SR architectures. We extend the LAM framework for volumetric SR and visualize the range of involved input voxels for all volumetric SR models. Fig. 7 shows a visual comparison of the LAM results using three sample volumes from the FACTS-Synth dataset at $\times 4$ upscaling. To visualize the contribution of each voxel, each LAM image shows the average contribution of each voxel throughout all slices of the prediction volume. The red regions highlight the input voxels contributing to the SR prediction volume marked by the red box, with higher intensities indicating a stronger voxel influence on the prediction output. We also report the diffusion index (DI), which is a measure of the overall range of involved voxels used to predict the SR output.

In contrast to LAM results reported in 2D SR [12, 16, 29], we find that there is a very sharp decline in contribution from input voxels outside the prediction volume for all models across all three sample volumes. This trend suggests that even in high-resolution datasets such as FACTS-Synth, local information is of relatively higher importance for volumetric SR than for 2D SR. Furthermore, we find that the degree to which the surrounding input voxels contribute to the SR prediction is highly dependent on the image structure inside the sample volume.

Our analysis finds no consistent top-performing model in terms of DI across the considered sample volumes. Given our experimental results in Tab. 1, we find no strong evidence correlating higher DI to higher PSNR/SSIM/NRMSE scores. Notably, we observe that for convolution models, the contribution of distant input voxels contribute progressively less to the SR output, whereas the LAM result of the transformer-based models SuperFormer and MTVNet reveals areas of high contribution far outside the prediction volume.

9. More visual comparisons

Fig. 8 shows more visual comparisons of SR predictions using the datasets HCP 1200, IXI, BraTS 2023, Kirby 21, FACTS-Synth and FACTS-Real at $\times 4$ upscaling. Across the four structural brain MRI datasets, our

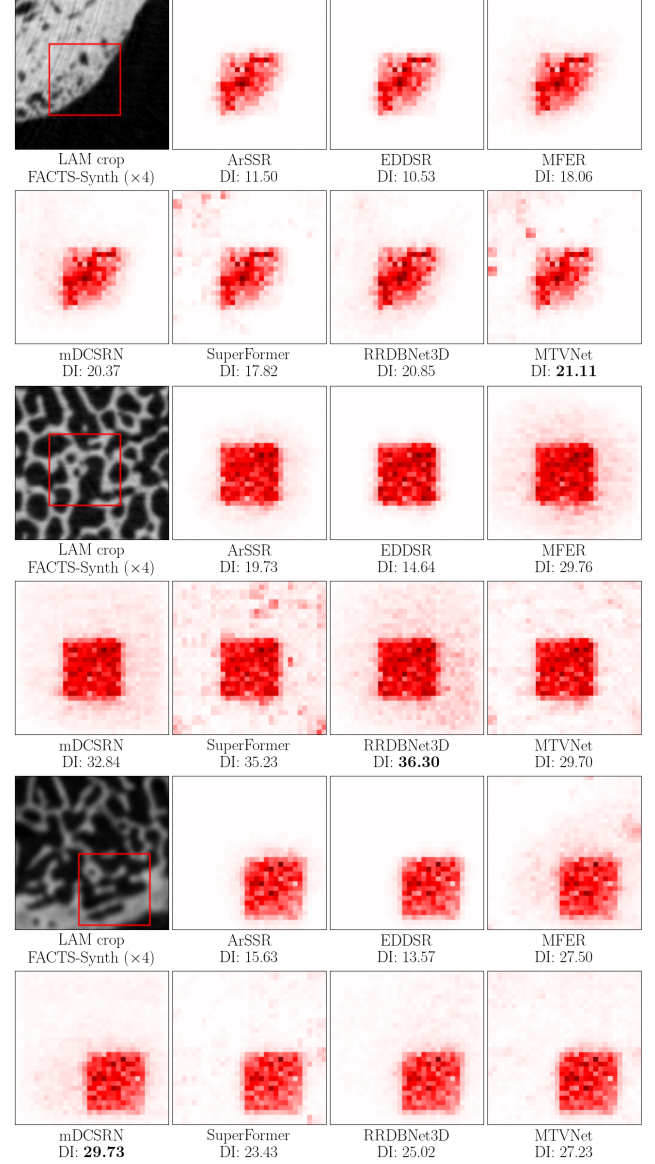


Figure 7. LAM comparisons of SR models using FACTS-Synth at $\times 4$ upscaling. Each LAM image shows the average contribution of each voxel throughout all slices of the prediction volume marked by the red box.

MTVNet produces noticeably sharper edges than ArSSR, EDDSR, MFER, mDCSRN, and SuperFormer while performing on par with RRDBNet3D. In FACTS-Real, the other transformer-based model SuperFormer reproduces texture artifacts not seen in the ground truth image. Our MTVNet avoids these artifacts while producing a less blurry SR prediction.

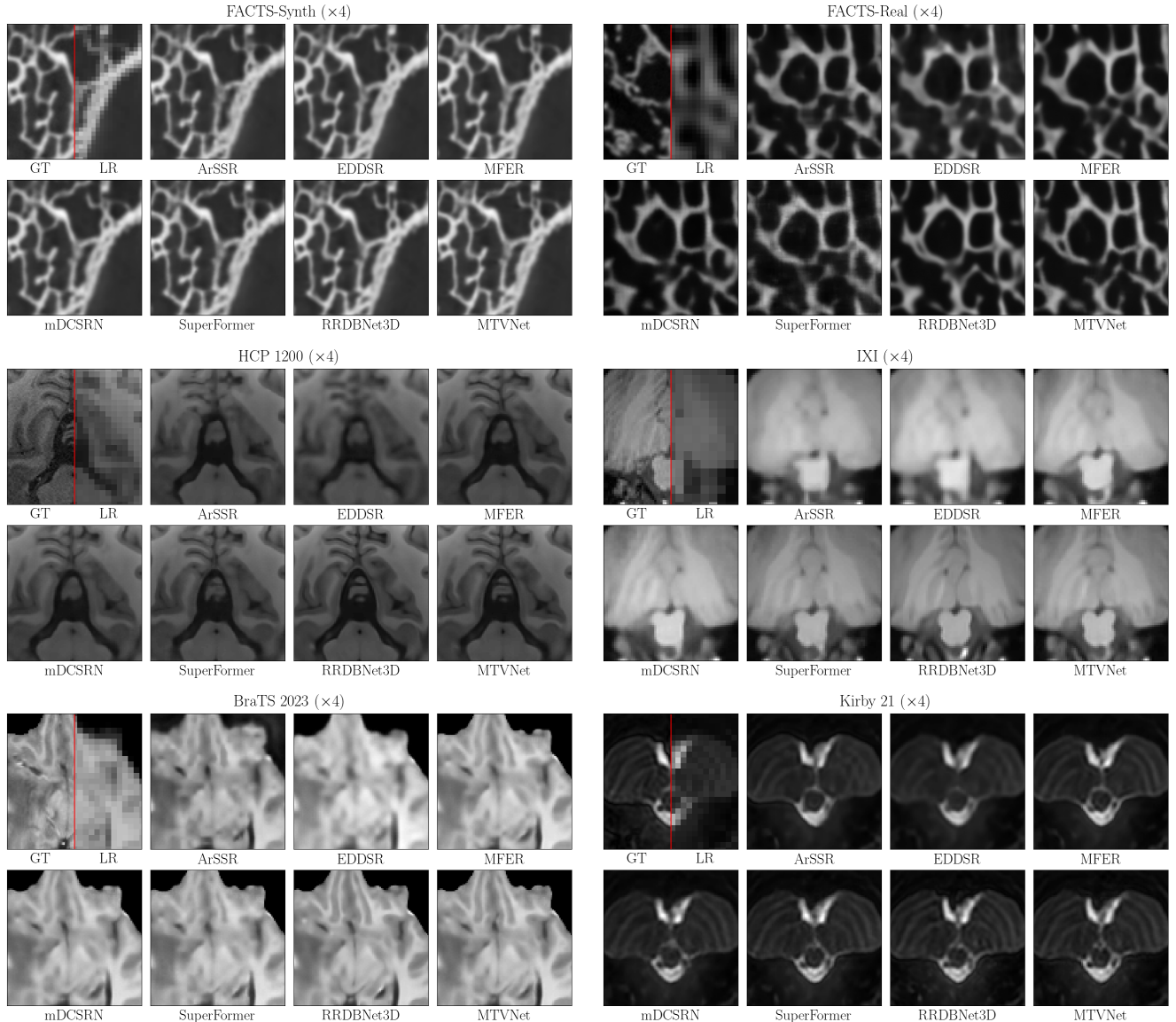


Figure 8. Visual comparisons of SR model outputs from the datasets HCP 1200, IXI, BraTS 2023, Kirby 21, FACTS-Synth, and FACTS-Real using 4 \times upscaling. The ground truth (GT) and LR input images are shown side-by-side in the top-left separated by the red line.